

Unravelling multi-temperature dust populations in the dwarf galaxy Holmberg II

Olag Pratim Bordoloi,¹* Yuri A. Shchekinov,²† P. Shalima,³‡ M. Safonova⁴§ and Rupjyoti Gogoi¹¶

¹Tezpur University, Napaam, Assam, India, 784028

²Raman Research Institute, Bengaluru, India, 560080

³Manipal Centre for Natural Sciences, Centre of Excellence, Manipal Academy of Higher Education, Manipal, Karnataka, India, 576104

⁴Indian Institute of Astrophysics, Bengaluru, India, 560034

Accepted XXX. Received YYY; in original form ZZZ

ABSTRACT

Holmberg II – a dwarf galaxy in the nearby M81 group – is a very informative source of distribution of gas and dust in the interstellar discs. High-resolution observations in the infrared (IR) allows us to distinguish isolated star-forming regions, photodissociation (PDR) and HII regions, remnants of supernovae (SNe) explosions and, as such, can provide information about more relevant physical processes. In this paper we analyse dust emission in the wavelength range 4.5 to 160 μm using the data from IR space observatories at 27 different locations across the galaxy. We observe that the derived spectra can be represented by multiple dust populations with different temperatures, which are found to be independent of their locations in the galaxy. By comparing the dust temperatures with the far ultraviolet (FUV) intensities observed by the UVIT instrument onboard AstroSat, we find that for locations showing a 100 μm peak, the temperature of cold (20 to 30 K) dust grains show a dependence on the FUV intensities, while such a dependence is not observed for the other locations. We believe that the approach described here can be a good tool in revealing different dust populations in other nearby galaxies with available high spatial resolution data.

Key words: galaxies: dwarf – ISM: dust, extinction – ISM: H II regions

1 INTRODUCTION

Dwarf galaxies (DG) – galaxies with baryonic mass of $M_b \sim 10^9 M_\odot$, are commonly thought to be the building blocks for the entire hierarchy of mass distribution in the Universe, being progressed during its evolution since post-recombination epochs through merging process (White & Rees 1978). Within this concept, DG in local Universe can serve as laboratories for understanding the details of physical processes regulating formation of the very first galaxies in early Universe (see review by Tolstoy et al. 2009, and more recent discussions in Henkel et al. (2022); Annibali & Tosi (2022)). Among the most important traits of DGs are their metal-poor interstellar medium (ISM) and, correspondingly, a low dust content (Henkel et al. 2022) – the features that are also commonly expected for early Universe galaxies. Observations of bright galaxies at $z > 10$ conducted first by the *Hubble Space Telescope* (HST), and subsequently by the *James Webb Space Telescope* (JWST), have indeed indicated a deficient amount of dust in a set of high- z galaxies (see discussion in Finkelstein et al. 2022; Ferrara et al. 2023).

In order for local DGs to indeed provide relevant information for understanding of their more distant congeners, the comparative analysis of their global emission characteristics, along with the respective

properties on smaller scales, is of a high importance (relevant discussion can be found in Izotov et al. 2021; Henkel et al. 2022). A good example of a DG in local Universe is the Holmberg II (Ho II) galaxy belonging to the nearby M81 group at a distance of ≈ 3.4 Mpc. Its modest inclination angle ($\approx 27^\circ$; Sánchez-Salcedo et al. (2014)) makes Ho II a very informative source of distribution of gas and dust in the interstellar discs. Spitzer and Herschel space telescopes with the angular resolution of $\sim 2'' - 5''$ can probe the Ho II interstellar disc with a high scrutiny. Scanning the interstellar medium (ISM) with such resolution can allow to distinguish isolated star forming regions (SFR), photodissociation (PDR) and HII regions, supernovae remnants, and can provide information about relevant physical processes. In this *Letter* we analyze spectra of dust emission in the range $\lambda\lambda = 4.5, \dots, 160 \mu\text{m}$ from Spitzer and Herschel archival data, focusing on a few rather small-area locations. It allows us to distinguish IR emission which cannot be attributed to the isothermal dust, thus requiring existence of at least two populations of dust with different temperatures.

Since the primary source of dust heating is the absorption of UV/optical photons by the dust grains, we have also utilised the highest available resolution ($1.2'' - 1.6''$) FUV observations of Ho II galaxy obtained by the UVIT instrument of India’s AstroSat mission (Singh et al. 2014) as part of this study. The data correspond to 3 epochs in 2016, 2 epochs in 2019, and 3 epochs in 2020 (Vinokurov et al. 2022). These observations are crucial in understanding the UV radiation fields, responsible for modifying the dust populations and their thermal IR emission profiles at these locations.

* olagpratim@gmail.com

† yuri.and.s@gmail.com

‡ shalima.p@gmail.com

§ margarita.safonova62@gmail.com

¶ rupjyotigogoi@gmail.com

2 OBSERVATIONAL DATA

We obtained the IR images of Ho II from two surveys, namely the SINGS survey (Kennicutt et al. 2003) and the KINGFISH survey (Kennicutt et al. 2011), archived at NASA/IPAC Infrared Science Archive, at 8 different wavelengths¹. 3.6 μm , 4.5 μm , 5.8 μm , and 8 μm images were obtained by the IRAC (Infrared Array Camera) instrument of Spitzer Space Telescope², while the MIPS (Multiband Imaging Photometer for Spitzer) instrument³ provided 24 μm , 70 μm , and 160 μm images. The 100 μm image was obtained by the PACS (Photodetector Array Camera and Spectrometer) instrument onboard Herschel Space Observatory. A constant background level was already subtracted from each of the images.

The images were further corrected to account for stellar contamination. For that we aligned and convolved the images to the same point-spread function (PSF) using IRAF⁴ tasks `imalign` and `psfmatch`, respectively. The IR intensities were extracted from these aligned and convolved images at our selected locations by aperture photometry in 5''-radius circular apertures. To account for the stellar contamination, we follow the methodology outlined by Helou et al. (2004), by employing a scaling approach based on the assumption that the 3.6- μm emission represents the total stellar emission. We scaled down the 3.6 μm intensities by specific factors, i.e. 0.596, 0.399, 0.232 and 0.032 for 4.5 μm , 5.8 μm , 8 μm , and 24 μm , respectively. These scaled 3.6 μm intensities were then subtracted from the respective intensities from the convolved images at corresponding wavelengths, which allowed us to isolate what we refer to as ‘diffuse dust emission’.

No correction for stellar contamination was applied to 70 μm , 100 μm , and 160 μm images, as stellar contribution diminishes rapidly with increasing wavelength in the IR, and thus can be considered negligible in this range. Interestingly, we observed the lack of 8 μm emission in most regions, in line with the proposed deficiency of polycyclic aromatic hydrocarbons (PAH) in this galaxy (Li 2020), except in three specific locations. Furthermore, the locations where IR emission was not detected in the range of wavelengths considered here were removed, resulting in a final sample of 27 locations. The IR intensities of this final set of locations, along with their respective errors, are presented in Table 1 and displayed on the FUV image taken on December 9, 2016 in Fig. 1. FUV intensities at these selected locations, extracted using the same 5''-radius aperture, showed to be approximately in the range of $(1.5 - 28) \times 10^{-10} \text{ ergs cm}^{-2} \text{ s}^{-1} \text{ sr}^{-1} \text{ \AA}^{-1}$. A more detailed analysis of the FUV emission in Ho II will be presented in the forthcoming paper (Bordoloi et al. 2023, in preparation).

3 RESULTS AND ANALYSIS

Locations depicted in Table 1, and displayed in Fig. 1, can be broadly classified into the following categories:

- (i) Locations with a peak intensity around 100 μm . The intensities

¹ To access SINGS and KINGFISH data, visit <https://irsa.ipac.caltech.edu/data/SPITZER/SINGS/galaxies/hoii/> and <https://irsa.ipac.caltech.edu/data/Herschel/KINGFISH/galaxies/HoII/PACS/>, respectively.

² see Fazio et al. (2004) for details about IRAC instrument.

³ see Rieke et al. (2004) for details about MIPS instrument.

⁴ IRAF is distributed by the National Optical Astronomy Observatory, which is operated by the Association of Universities for Research in Astronomy, Inc., under a cooperative agreement with the National Science Foundation.

of these locations after 100 μm show a decreasing trend towards longer wavelengths.

- (ii) Locations with peak intensity around 70 μm . The intensities, after peaking around 70 μm , mostly decrease towards 100 μm , and then again show an increasing trend towards 160 μm .

- (iii) Locations corresponding to HI voids. These voids are the regions where the neutral hydrogen column density $N(\text{HI})$ is less than $1 \times 10^{21} \text{ cm}^{-2}$ (Walter et al. 2007). The intensities of these locations typically peak at 70 μm , and then experience a dip at 100 μm .

- (iv) Locations with an additional emission at 8 μm . The intensity of these locations peaks around 100 μm and decreases towards longer wavelengths, similar to the locations in category (i).

3.1 Dust in Holmberg II

A comprehensive study of dust properties in their interplay with other physical characteristics in Holmberg II galaxy among other M81 dwarf galaxies is given by Walter et al. (2007). The IR brightness at 24, 70, and 160 μm has been found to correlate with HI distribution, though with rather patchy and sparse distribution of the dust emission, which is either assembled into great complexes, or because it is heated by localized sources, such as HII regions, SNe, or stellar wind shocks (e.g., Fig. 2 in Walter et al. 2007, see also discussion in Galliano et al. (2018)). Following Galliano et al. (2021) and Egorov et al. (2023), the latter would result in a suppressed emission in PAH molecules. This is consistent with the conclusion by Walter et al. (2007) that PAH features at 8 μm and 11.3 μm in Ho II contribute only around ~ 0.1 as compared to the continuum – nearly 20 times lower than in their template galaxy NGC 7552. It is worth noting in this respect that the gas scale height in Ho II is around 200 pc (Banerjee et al. 2011) and, accounting for the fact that the galaxy has a rather modest SFR of $\Sigma_{\text{SFR}} \sim 0.016 M_{\odot} \text{ yr}^{-1} \text{ kpc}^{-2}$ (Walter et al. 2007), one can conclude that all mechanical energy from stellar activity is locked within the ISM disc without expulsion of it outside (Nath & Shchekinov 2013). This can result in an enhanced anticorrelation between the SFR and PAH abundance in dwarf galaxies with low gas scale heights (for more discussion, see Galliano et al. 2018, 2021).

On the other hand, patchiness in spatial distribution of dust in Ho II can be connected with an exceptionally low amount of dust, $M_d/M_{\text{HI}} \sim 3 \times 10^{-4}$, which is ~ 20 times lower than in spirals (see Fig. 11a in Walter et al. 2007), being consistent with its low gas metallicity, $12 + \log(\text{O}/\text{H}) \simeq 7.68$ (see panel *d*) on Fig. 8 in Galliano et al. (2021). With $M_{\text{HI}} \sim 6 \times 10^8 M_{\odot}$, this gives $M_d \sim 2 \times 10^5 M_{\odot}$.

More recently, (Zhou et al. 2016, see their Fig. 2) payed attention to a principally different spectral shape of dust emission in metal deficient ($12 + \log[\text{O}/\text{H}] \leq 7.65$) dwarf galaxies, Ho II among them, as compared to the galaxies with higher metallicity – their colours, the ratios $[\nu F_{\nu}]_{70 \mu\text{m}}/[\nu F_{\nu}]_{160 \mu\text{m}}$ vs. $[\nu F_{\nu}]_{160 \mu\text{m}}/[\nu F_{\nu}]_{250 \mu\text{m}}$, look shifted towards lower values of the spectral index $\beta < 1$. We found this tendency in the Ho II galaxy on a colour–colour diagram $[\nu F_{\nu}]_{24 \mu\text{m}}/[\nu F_{\nu}]_{70 \mu\text{m}}$ vs. $[\nu F_{\nu}]_{70 \mu\text{m}}/[\nu F_{\nu}]_{100 \mu\text{m}}$, representing the dust at different locations in its disc (Fig. 2). It is clearly seen that some locations concentrate beyond the domain of positive spectral index $\beta \geq 0$. No less striking are also outliers with $[\nu F_{\nu}]_{24 \mu\text{m}}/[\nu F_{\nu}]_{70 \mu\text{m}} \sim 0.05$ and $[\nu F_{\nu}]_{70 \mu\text{m}}/[\nu F_{\nu}]_{100 \mu\text{m}}$, being as high as ~ 10 . In this regard, it is remarkable that these outliers come from the locations selected through different, though not mutually excluding, criteria. Locations marked in red represent regions deficient in atomic hydrogen ($N(\text{HI}) < 10^{21} \text{ cm}^{-2}$), in green – those where IR spectra peak at 70 μm , and in cyan – locations where spectra peak at 100 μm . Draine & Li (2007) showed that stochastically

Table 1. Details of *Spitzer* IR observations. This is a sample of first few entries of the table; the full table is available online.

Location No	l (degrees)	b (degrees)	$I_{4.5\mu\text{m}}$ (MJy sr $^{-1}$)	$I_{5.8\mu\text{m}}$ (MJy sr $^{-1}$)	$I_{8\mu\text{m}}$ (MJy sr $^{-1}$)	$I_{24\mu\text{m}}$ (MJy sr $^{-1}$)	$I_{70\mu\text{m}}$ (MJy sr $^{-1}$)	$I_{100\mu\text{m}}$ (MJy sr $^{-1}$)	$I_{160\mu\text{m}}$ (MJy sr $^{-1}$)
1	144.2731	32.6844	0.0106 ± 0.0273	0.0330 ± 0.0158	0 ± 0.0141	0.0333 ± 0.0100	1.9079 ± 0.0742	0.2300 ± 0.526	3.5553 ± 0.3761
2	144.2898	32.6750	0.0069 ± 0.0075	0.0200 ± 0.0079	0 ± 0.0062	0.1092 ± 0.0121	5.2336 ± 0.4443	7.2000 ± 0.5544	3.8332 ± 0.4575
3	144.2512	32.6607	0.0055 ± 0.0015	0.0122 ± 0.0035	0 ± 0.0065	0.6279 ± 0.1453	7.7358 ± 1.2877	14.4400 ± 2.5546	1.6263 ± 0.5952
4	144.2952	32.7203	0.0114 ± 0.0016	0.0191 ± 0.0035	0 ± 0.0043	0.3012 ± 0.0467	5.9099 ± 0.1316	8.7800 ± 0.8157	3.7606 ± 0.1606
5	144.2699	32.6985	0.0098 ± 0.0068	0.0340 ± 0.0064	0 ± 0.0053	0.1225 ± 0.0153	4.5948 ± 0.4802	1.9600 ± 0.4780	4.5118 ± 0.3977
6	144.2882	32.6942	0.0112 ± 0.0038	0.0245 ± 0.0037	0 ± 0.0045	0.0694 ± 0.0077	1.8620 ± 0.1317	2.4400 ± 0.4311	2.8699 ± 0.0896
7	144.2960	32.6858	0.0053 ± 0.0023	0.0171 ± 0.0040	0 ± 0.0041	0.0376 ± 0.0119	2.3811 ± 0.1101	3.8800 ± 0.3801	3.0756 ± 0.2645
8	144.2816	32.6822	0.0183 ± 0.0218	0.0619 ± 0.0147	0.0393 ± 0.0217	0.3235 ± 0.0269	5.0719 ± 0.3350	10.6100 ± 0.4589	5.0871 ± 0.0997

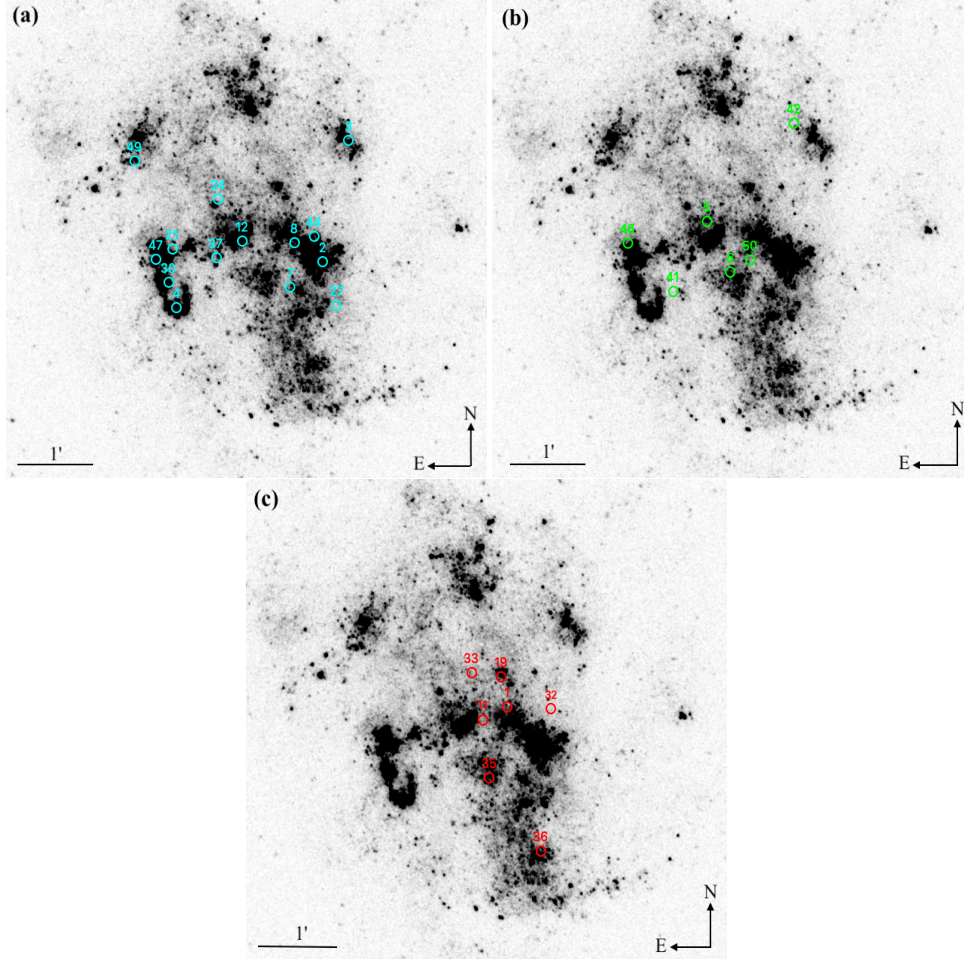


Figure 1. Locations depicted in Table 1 overlotted on the FUV image of Ho II obtained by the UVIT instrument (Vinokurov et al. 2022). (a) Locations where intensity peaks at 100 μm , represented by cyan colour, mostly lie in the SFR, (b) Locations where intensity peaks at 70 μm , represented by green colour, lie mostly in the outskirts of SFR, (c) Locations lying in HI voids ($N(\text{HI}) < 1 \times 10^{21} \text{ cm}^{-2}$, Walter et al. (2007)), represented by red colour. The circles representing the locations are of the same size as circular apertures ($5''$ radius) used to extract the IR intensities from the locations. The FUV image was taken on December 9, 2016 with an exposure time of around 9 ks.

heated small dust grains can contribute to an excessive 70 μm emission provided there is a sufficiently high UV energy density. However, as mentioned above, Ho II is apparently deficient in small size grains and PAHs, and therefore in this case the emission could be due to stochastic heating of large dust grains by shock waves from stellar winds and SNe (Dwek 1986, see also latest examples in Drozdov & Shchekinov (2019); Drozdov (2021)). One therefore can assume that the outliers shown in Fig. 2 represent dust clumps heated by the shocks.

3.2 Multi-temperature dust spectra

In this *Letter* we interpret the differences observed in loosely selected IR sources in Sec. 3 as due to contributions from multi-temperature dust components that originate in distinct regions within the same field of view (FOV) under the dust heating from different not always resolved sources.

The observed flux density from a cloud containing dust of total

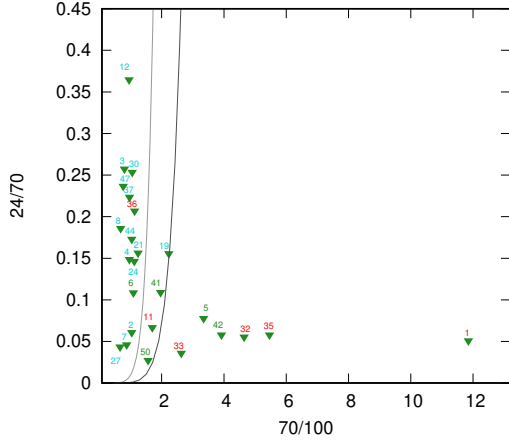


Figure 2. $[\nu F_\nu]_{24 \mu\text{m}}/[\nu F_\nu]_{70 \mu\text{m}}$ vs. $[\nu F_\nu]_{70 \mu\text{m}}/[\nu F_\nu]_{100 \mu\text{m}}$ color-color diagram for the set of locations selected in this paper. Outliers towards high $[\nu F_\nu]_{70 \mu\text{m}}/[\nu F_\nu]_{100 \mu\text{m}}$ are apparently due to an enhanced $70 \mu\text{m}$ emission. Thin grey line shows the ratio for $\beta = 0$ (black body), thick darker line is for $\beta = 2$, temperature changes from 3 K to 700 K from the bottom to top. Numbers and their colours correspond to locations shown in Fig. 1.

mass M_d at frequency ν is given by (see [Hildebrand 1983](#)),

$$F_\nu = \frac{3M_d}{4\pi a \rho_d D^2} Q(a, \nu) B_\nu(T), \quad (1)$$

where a is the dust grain radius (assumed $a \sim 0.1 \mu\text{m}$), ρ_d is the density of the dust material, $B_\nu(T)$ the Planck function, and D is the detector–cloud separation. $Q(a, \nu) \approx 0.01 a (\nu/c)^\alpha$ is the emissivity where a and ν are in cgs units. [Dwek & Arendt \(1992\)](#) assume a spectral index $\alpha = 1.94$, though a wider range of $\alpha = 1.5 - 2$ is commonly applied (e.g. [Draine & Lee 1984](#); [Cortese et al. 2012](#)). For the sake of simplification of the fitting procedure and accounting of observational uncertainties, we assume $\alpha = 2$, unless specified.

Fig. 3 illustrates several examples of the IR spectra observed in 4 specific locations of Ho II galaxy (these locations are marked in Fig. 1). The fitting procedure is applied to the spectra in a given FOV within the error bars, with free variables being the dust temperature T_d and dust mass M_d under fixed spectral index $\beta = 2$. The dust mass M_d is reduced to the surface dust mass within the corresponding aperture with solid angle $\Delta\Omega$. Therefore, the fitting outcome is the dust temperature T_d , the dust mass M_d for warm and hot ($T_d > 30$ K) dust components, being presumably compact dusty structures, and the surface dust mass Σ_d for colder ($T_d < 30$ K) dust redistributed most likely in diffuse ISM.

From the estimates one can preliminarily conclude that *i*) cold dust at $T_d \approx 10 - 30$ K is from the diffuse ISM with a dust-to-gas mass fraction, $\zeta_d = (2 - 3) \times 10^{-3}$ which is consistent with an order of magnitude lower metallicity, in estimates a gas scale height of $z_0 = 200$ pc and in the plane gas density of $n = 1 \text{ cm}^{-3}$ are assumed, *ii*) dust at 30 to 50 K can apparently stem from the ISM in close vicinity of individual stars. The inferred surface dust mass density for the colder $T_d < 30$ K components is on average $\langle \Sigma_d \rangle \sim (1 - 3) \times 10^{-3} M_\odot \text{ pc}^{-2}$ and results in the total dust mass within $1.5'$ diameter of Ho II to be around $\sim (1 - 30) \times 10^4 M_\odot$, which is consistent with [Walter et al. \(2007\)](#). The ‘high-temperature’ peaks with $T_d > 220$ K require apparently alternative energy sources, such as the IR emission from dusty envelopes around red giants ([Jura 1999](#); [Lagadec et al. 2005](#)), circumstellar discs ([Uzpen et al. 2008](#)), as well as dusty clumps in wind-blown bubbles and SNe.

Heating by stellar UV/FUV photons looks unphysical because the required energy density νu_ν is as high as $\sim 10^7$ of Habing value $\nu u_{\nu,0} = 4 \times 10^{-14} \text{ erg cm}^{-3}$, the standard interstellar radiation field (Sec. 12.5 in [Draine 2011](#)).

4 DISCUSSION AND CONCLUSIONS

4.1 Discussion

Detailing of dust thermal emission on smaller spatial scales allows us to avoid blurring and confusing effects caused by averaging over the larger areas and mixing contributions from sources with different physical characteristics. Such a high resolution scrutiny is provided by the Spitzer and Herschel space telescopes in the nearby dwarf Ho II galaxy. Its relatively small inclination allows to recognize contributions from rather small scale features without considerable mixing that can originate along sight of lines in a crowd environment. It is worth noting that this approach, once completed, promises a good tool for revealing different dust populations in other nearby galaxies where high spatial resolution is reachable (e.g., M31, LMC, SMC, and other DGs in the Local Group).

In this *Letter*, amongst the IR spectra at locations of visually different nature as described above (see Fig. 3 and a brief description in the caption), we recognized cloud(let)s with evidently different spectra, although not connected directly to differences between the three groups of sources shown in Fig. 1. For instance, IR spectra in HI voids do not show obvious distinct features. In compact regions lying very close to the FUV bright spots, presumably associated with active star formation (although not always being tightly connected with bright H α regions resolved by the HST as, e.g., locations 8, 44 and 49), we have identified three populations of cloudlets with apparently cold, warm, and hot components. Within the simplest assumptions, we attributed these differences to different temperatures. Following [Walter et al. \(2007\)](#), we have neglected the contribution from PAH molecules. The primary physical reason for such an approximation is that PAH molecules are very fragile under strong FUV radiation (see for recent discussions [Egorov et al. 2023](#), and references therein).

It seems natural to assume that the coldest dust components are distributed diffusely throughout the ISM and are heated by the FUV radiation field. Surprisingly, preliminary inspection of possible connection of the cold dust population with the FUV radiation field has shown no obvious signs of correlation for most of the locations (Fig. 4). It is seen that temperatures of the cold dust components in HI voids, and in locations with spectra peaking at $70 \mu\text{m}$, range between $10 - 20$ K and are not correlated with FUV intensity. However, the dust component of the sample with the peak intensity at $100 \mu\text{m}$ shows slightly higher temperatures $\approx 20 - 30$ K growing with the FUV intensity.

It is pertinent to note that in the cleaned spectra with the flux at $8 \mu\text{m}$ being clearly above the detection limit (locations 8, 12, 37 in Table 1), we detect signs of enhanced intensity at wavelengths near those that are typically attributed to PAH features, i.e. $\sim 3.3 \mu\text{m}$, $\sim 6 \mu\text{m}$, and $\sim 24 \mu\text{m}$. It is also worth noting that emission in this wavelength range is widely present in PDRs due to the main H $_2$ rotational lines at $\lambda\lambda = 6.9, \dots, 17.0 \mu\text{m}$ ([Compiègne et al. 2008](#)). However, in the case of Ho II, we did not find any reference in the literature to these features being detected or studied. We are not aware of any reported data on these spectral features in this wavelength range for Ho II galaxy since 2010. Therefore, within the above assumptions and following the arguments by [Walter et al. \(2007\)](#); [Egorov et al. \(2023\)](#), we approximated the spectra in this

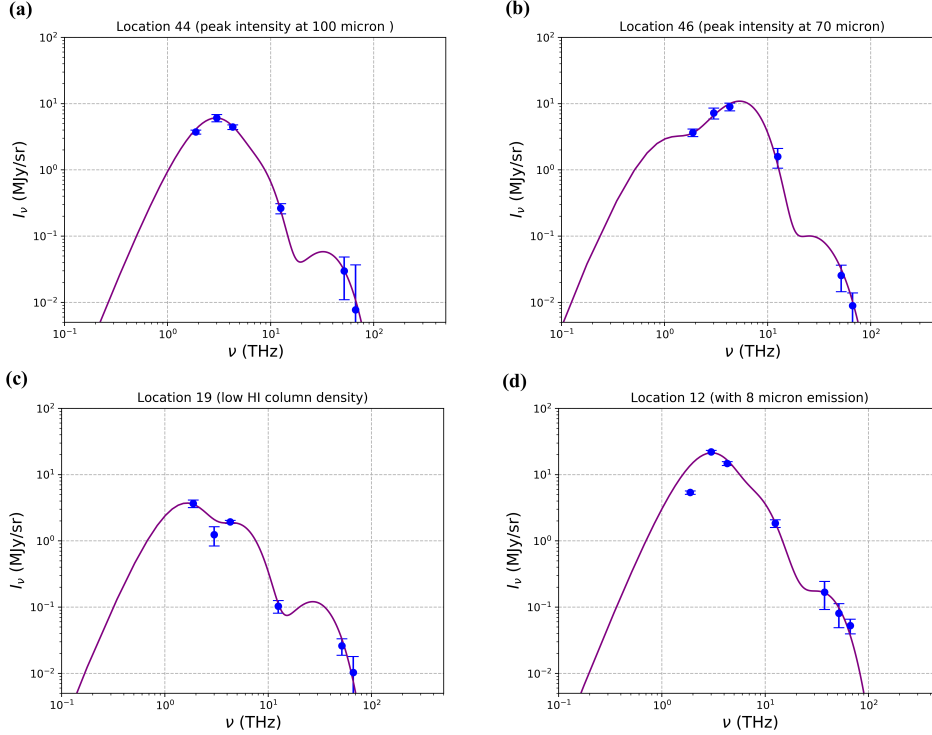


Figure 3. Fits of the spectra of dust at different environmental conditions as classified in Fig. 1. They represent spectra of dust: **i)** spectra peaking at 100 μm , **ii)** spectra peaking at 70 μm , **iii)** in regions with HI column densities below the detection limit $N(\text{HI}) < 10^{21} \text{ cm}^{-2}$, **iv)** spectra with emission at 8 μm , **v)** spectra with a weak intensity dip at 100 μm and **vi)** spectra with a strong intensity dip at 100 μm . Specifically, the presented spectra fitted with multi-temperature modified black body with the following temperatures and dust surface mass densities for cold components and dust masses for warm and hot ones: (a) $T = 27, 56, 310 \text{ K}$ ($\Sigma_d = 6 \times 10^{-5} M_\odot \text{ pc}^{-2}$, $M_d = 0.009, 6.4 \times 10^{-8} M_\odot$); (b) $T = 10, 25, 53, 220, 320 \text{ K}$ ($\Sigma_d = 3 \times 10^{-3} M_\odot \text{ pc}^{-2}$, $M_d = 0.5, 0.08, 4 \times 10^{-7}, 4 \times 10^{-8} M_\odot$); (c) $T = 15, 46, 260 \text{ K}$ ($\Sigma_d = 7 \times 10^{-4} M_\odot \text{ pc}^{-2}$, $M_d = 0.025, 3 \times 10^{-7} M_\odot$); (d) $T = 28, 63, 100, 320 \text{ K}$ ($\Sigma_d = 6 \times 10^{-4} M_\odot \text{ pc}^{-2}$, $M_d = 63, 0.002, 2 \times 10^{-7} M_\odot$).

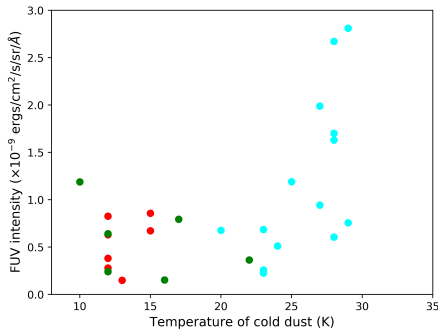


Figure 4. Variation of temperature of cold dust with FUV intensity for the considered 27 locations. Colour coding is according to Fig. 1.

wavelength range by a modified black body from sources with higher temperatures. We attribute them to compact energy sources like dusty envelopes around red giant stars, including possibly, carbon stars, and dusty clumps heated by shock waves from stellar wind or SNe.

4.2 Conclusions

(i) We present for the first time analysis of IR dust emission in the galaxy Holmberg II to detect spatial variations of dust parameters on small physical scales of $\sim 82 \text{ pc}$ (corresponding to a circular area

of $5''$ -radius) using high angular resolution data from Spitzer and Herschel.

(ii) In several locations, connected to physically distinct regions, we found spectra that can represent several – up to five, dust populations with different temperatures. Spectral characteristics are not sensitive to the HI column density, except for the cold dust component with $T_d = 10 - 15 \text{ K}$ which concentrates predominantly in HI deficient regions. Preliminary inspection shows that this cold dust population does not show a dependence on FUV intensity.

(iii) Similarly, the cold dust in those regions with spectra peaking at 70 μm has temperatures nearly in the same range as the HI voids with little dependence on FUV intensity. However, for those locations with the peak intensity at 100 μm , the temperature of the cold dust component ($T_d = 20 - 30 \text{ K}$) increases with FUV intensity.

(iv) The estimated dust mass manifests signs of anti-correlation with its temperature, as formerly reported for dwarf star-forming galaxies by Izotov et al. (2014).

ACKNOWLEDGEMENTS

OPB and RG are thankful to Science & Engineering Research Board (SERB), Department of Science & Technology (DST), Government of India for financial support (EMR/2017/003092). OPB acknowledges the help received during this work from his colleagues Anshuman Borgohain and Hritwik Bora. SP acknowledges Manipal Centre for Natural Sciences, Centre of Excellence, Manipal Academy of Higher Education (MAHE) for facilities and support. MS ac-

knowledges the financial support by the DST, Government of India, under the Women Scientist Scheme (PH) project reference number SR/WOS-A/PM-17/2019. YS acknowledges the hospitality of the Raman Research Institute, Bengaluru, India.

DATA AVAILABILITY

The data (complete Table 1 and an additional table on the insights to the selected locations) associated with this manuscript are available at the following website: <https://github.com/olagpratim/Details-of-Spitzer-IR-observations/blob/a9b835647bfbe02f85f2fd4e75abb6e145dd095b/AppendixA.pdf>

REFERENCES

- Annibali F., Tosi M., 2022, *Nature Astronomy*, **6**, 48
- Banerjee A., Jog C. J., Brinks E., Bagetakos I., 2011, *MNRAS*, **415**, 687
- Bordoloi O. P., Shalima P., Safonova M., Shchekinov Y., Gogoi R., 2023, in preparation
- Compiègne M., Abergel A., Verstraete L., Habart E., 2008, *A&A*, **491**, 797
- Cortese L., et al., 2012, *A&A*, **540**, A52
- Draine B. T., 2011, *Physics of the Interstellar and Intergalactic Medium*
- Draine B. T., Lee H. M., 1984, *ApJ*, **285**, 89
- Draine B. T., Li A., 2007, *ApJ*, **657**, 810
- Drozdov S. A., 2021, *Astrophysics*, **64**, 126
- Drozdov S. A., Shchekinov Y. A., 2019, *Astrophysics*, **62**, 540
- Dwek E., 1986, *ApJ*, **302**, 363
- Dwek E., Arendt R. G., 1992, *ARA&A*, **30**, 11
- Egorov O. V., et al., 2023, *ApJ*, **944**, L16
- Fazio G. G., et al., 2004, *ApJS*, **154**, 10
- Ferrara A., Pallottini A., Dayal P., 2023, *MNRAS*, **522**, 3986
- Finkelstein S. L., et al., 2022, *ApJ*, **940**, L55
- Galliano F., Galametz M., Jones A. P., 2018, *ARA&A*, **56**, 673
- Galliano F., et al., 2021, *A&A*, **649**, A18
- Helou G., et al., 2004, *ApJS*, **154**, 253
- Henkel C., Hunt L. K., Izotov Y. I., 2022, *Galaxies*, **10**, 11
- Hildebrand R. H., 1983, *QJRAS*, **24**, 267
- Izotov Y. I., Guseva N. G., Fricke K. J., Krügel E., Henkel C., 2014, *A&A*, **570**, A97
- Izotov Y. I., Guseva N. G., Fricke K. J., Henkel C., Schaerer D., Thuan T. X., 2021, *A&A*, **646**, A138
- Jura M., 1999, *ApJ*, **515**, 706
- Kennicutt Robert C. J., et al., 2003, *PASP*, **115**, 928
- Kennicutt R. C., et al., 2011, *PASP*, **123**, 1347
- Lagadec E., Mékarnia D., de Freitas Pacheco J. A., Dougados C., 2005, *A&A*, **433**, 553
- Li A., 2020, *Nature Astronomy*, **4**, 339
- Nath B. B., Shchekinov Y., 2013, *ApJ*, **777**, L12
- Rieke G. H., et al., 2004, *ApJS*, **154**, 25
- Sánchez-Salcedo F. J., Hidalgo-Gómez A. M., Martínez-García E. E., 2014, *Rev. Mex. Astron. Astrofis.*, **50**, 225
- Singh K. P., et al., 2014, in Takahashi T., den Herder J.-W. A., Bautz M., eds, *Society of Photo-Optical Instrumentation Engineers (SPIE) Conference Series Vol. 9144, Space Telescopes and Instrumentation 2014: Ultraviolet to Gamma Ray*. p. 91441S, doi:10.1117/12.2062667
- Tolstoy E., Hill V., Tosi M., 2009, *ARA&A*, **47**, 371
- Uzpen B., Koblunicky H. A., Semler D. R., Bensby T., Thom C., 2008, *ApJ*, **685**, 1157
- Vinokurov A., et al., 2022, *Astrophysical Bulletin*, **77**, 231
- Walter F., et al., 2007, *ApJ*, **661**, 102
- White S. D. M., Rees M. J., 1978, *MNRAS*, **183**, 341
- Zhou L., Shi Y., Diaz-Santos T., Armus L., Helou G., Stierwalt S., Li A., 2016, *MNRAS*, **458**, 772

Table A1. IR intensities in selected 27 locations. Colour coding is according to Fig. 1. See Sec. 2 for details of calculations.

Location No	l (degrees)	b (degrees)	$I_{4.5\mu\text{m}}$ (MJy sr ⁻¹)	$I_{5.8\mu\text{m}}$ (MJy sr ⁻¹)	$I_{8\mu\text{m}}$ (MJy sr ⁻¹)	$I_{24\mu\text{m}}$ (MJy sr ⁻¹)	$I_{70\mu\text{m}}$ (MJy sr ⁻¹)	$I_{100\mu\text{m}}$ (MJy sr ⁻¹)	$I_{160\mu\text{m}}$ (MJy sr ⁻¹)
1	144.2731	32.6844	0.0106 ± 0.0273	0.0330 ± 0.0158	0 ± 0.0141	0.0333 ± 0.0100	1.9079 ± 0.0742	0.2300 ± 0.526	3.5553 ± 0.3761
2	144.2898	32.6750	0.0069 ± 0.0075	0.0200 ± 0.0079	0 ± 0.0062	0.1092 ± 0.0121	5.2336 ± 0.4443	7.2000 ± 0.5544	3.8332 ± 0.4575
3	144.2512	32.6607	0.0055 ± 0.0015	0.0122 ± 0.0035	0 ± 0.0065	0.6279 ± 0.1453	7.7358 ± 1.2877	14.4400 ± 2.5546	1.6263 ± 0.5952
4	144.2952	32.7203	0.0114 ± 0.0016	0.0191 ± 0.0035	0 ± 0.0043	0.3012 ± 0.0467	5.9099 ± 0.1316	8.7800 ± 0.8157	3.7606 ± 0.1606
5	144.2699	32.6985	0.0098 ± 0.0068	0.0340 ± 0.0064	0 ± 0.0053	0.1225 ± 0.0153	4.5948 ± 0.4802	1.9600 ± 0.4780	4.5118 ± 0.3977
6	144.2882	32.6942	0.0112 ± 0.0038	0.0245 ± 0.0037	0 ± 0.0045	0.0694 ± 0.0077	1.8620 ± 0.1317	2.4400 ± 0.4311	2.8699 ± 0.0896
7	144.2960	32.6858	0.0053 ± 0.0023	0.0171 ± 0.0040	0 ± 0.0041	0.0376 ± 0.0119	2.3811 ± 0.1101	3.8800 ± 0.3801	3.0756 ± 0.2645
8	144.2816	32.6822	0.0183 ± 0.0218	0.0619 ± 0.0147	0.0393 ± 0.0217	0.3235 ± 0.0269	5.0719 ± 0.3350	10.6100 ± 0.4589	5.0871 ± 0.0997
11	144.2757	32.6922	0.0094 ± 0.0045	0.0361 ± 0.0043	0 ± 0.0040	0.1135 ± 0.0067	4.9482 ± 0.3170	4.1600 ± 0.7900	1.8229 ± 0.7535
12	144.2774	32.6973	0.0527 ± 0.0132	0.0809 ± 0.0320	0.1682 ± 0.0759	1.8455 ± 0.2469	14.7611 ± 1.0000	22.1000 ± 1.2138	5.3792 ± 0.3122
19	144.2630	32.6846	0.0103 ± 0.0077	0.0261 ± 0.0073	0 ± 0.0054	0.1034 ± 0.0222	1.9352 ± 0.1041	1.2400 ± 0.4014	3.6667 ± 0.4822
21	144.2754	32.7183	0.0115 ± 0.0082	0.0327 ± 0.0056	0 ± 0.0059	0.5014 ± 0.1046	9.3478 ± 0.7582	10.7500 ± 0.3933	5.1692 ± 0.1822
24	144.2618	32.7021	0.0150 ± 0.0328	0.0467 ± 0.0212	0 ± 0.0142	0.1520 ± 0.0269	3.0249 ± 0.2186	3.8500 ± 0.6202	3.1424 ± 0.8492
27	144.3054	32.6733	0.0004 ± 0.0608	0.0216 ± 0.0361	0 ± 0.0205	0.0246 ± 0.0077	1.6464 ± 0.0832	3.5500 ± 0.4701	1.9316 ± 0.1883
30	144.2863	32.7213	0.0204 ± 0.0054	0.0278 ± 0.0070	0 ± 0.0089	0.7002 ± 0.0429	8.0550 ± 0.3701	10.9100 ± 0.4139	2.9251 ± 0.2354
32	144.2768	32.6716	0.0075 ± 0.0048	0.0249 ± 0.0049	0 ± 0.0048	0.0328 ± 0.0076	1.7242 ± 0.2066	0.5300 ± 0.4317	2.0164 ± 0.3426
33	144.2595	32.6931	0.0089 ± 0.0061	0.0408 ± 0.0052	0 ± 0.0058	0.0184 ± 0.0074	1.4919 ± 0.1011	0.8100 ± 0.3886	1.9019 ± 0.1035
35	144.2949	32.6935	0.0074 ± 0.0039	0.0372 ± 0.0062	0 ± 0.0045	0.0258 ± 0.0092	1.2994 ± 0.2115	0.3400 ± 0.4879	2.8701 ± 0.4514
36	144.3222	32.6821	0.0053 ± 0.0047	0.0048 ± 0.0046	0 ± 0.0040	0.0269 ± 0.0070	0.3790 ± 0.1105	0.4800 ± 0.3691	0.9162 ± 0.2116
37	144.2812	32.7059	0.0283 ± 0.0248	0.0783 ± 0.0157	0.0355 ± 0.0161	0.4197 ± 0.0166	4.7531 ± 0.1707	8.4700 ± 0.6406	5.6591 ± 0.2748
41	144.2905	32.7123	0.0065 ± 0.0032	0.0361 ± 0.0038	0 ± 0.0043	0.1141 ± 0.0109	3.0536 ± 0.3157	2.2200 ± 0.3941	2.5669 ± 0.1019
42	144.2438	32.6674	0.0029 ± 0.0022	0.0021 ± 0.0040	0 ± 0.0049	0.0256 ± 0.0064	1.2904 ± 0.1688	0.4700 ± 0.3980	1.2432 ± 0.3501
44	144.2809	32.6760	0.0077 ± 0.0293	0.0298 ± 0.0188	0 ± 0.0131	0.2634 ± 0.0461	4.4406 ± 0.3565	6.1000 ± 0.7717	3.7378 ± 0.2591
46	144.2714	32.7231	0.0089 ± 0.0050	0.0255 ± 0.0110	0 ± 0.0166	1.5858 ± 0.5204	8.9976 ± 1.1983	7.2400 ± 1.3546	3.6638 ± 0.4835
47	144.2778	32.7236	0.0231 ± 0.0045	0.0313 ± 0.0060	0 ± 0.0053	0.7442 ± 0.0395	9.7106 ± 0.5049	14.3700 ± 0.7789	5.2882 ± 0.1123
49	144.2435	32.7246	0.0119 ± 0.0831	0.0426 ± 0.0484	0 ± 0.0268	0.2938 ± 0.0202	1.8468 ± 0.1020	2.6500 ± 0.3166	1.7170 ± 0.0706
50	144.2854	32.6877	0.0039 ± 0.0026	0.0221 ± 0.0039	0 ± 0.0039	0.0306 ± 0.0075	3.2687 ± 0.3817	2.9900 ± 0.4238	3.0087 ± 0.4635

APPENDIX A: IR INTENSITIES AND ADDITIONAL DATA FOR SELECTED 27 LOCATIONS

Table A2. Additional insights to the selected locations.

Location No.	Nearby HII regions	Star forming complex ^a	Distance to the closest HII region (arcsec) ^b	Age of HII regions (Myr) ^c
Peak intensity at 100 μm				
2	HSK 10, 16, 20	NW	3.74 (HSK 20)	3.5 - 6.3
3	HSK 4, 6, 7		1.80 (HSK 7)	2.5 - 3.5, 4.5 - 6.3
4	HSK 61, 65, 67	SE	2.52 (HSK 65)	2.5 - 4.5
7	HSK 26	NW	3.96 (HSK 7)	3.5 - 4.5
21	HSK 71, 73	NE	4.15 (HSK 73)	2.5 - 3.5
24	HSK 50, 52	N	5.77 (HSK 50)	3.5 - 4.5
27	HSK 13	NW	6.13 (HSK 13)	2.5 - 3.5
44	HSK 15, 17	NW	2.17 (HSK 15)	3.5 - 6.3
30	HSK 63, 64, 70	SE	0.60 (HSK 70)	3.5 - 4.5
47	HSK 73, 74	NE	2.88 (HSK 74)	2.5 - 3.5
49	HSK 80, 81, 82	Ext NE	2.52 (HSK 80)	3.5 - 4.5
Peak intensity at 70 μm				
5	HSK 45	N	17.28 (HSK 45)	3.7 ^d
6	HSK 35	N	12.60 (HSK 35)	4.5 - 6.3
41	HSK 57, 58	SE	1.87 (HSK 58)	3.5 - 4.5
42	HSK 7		17.31 (HSK 7)	2.5 - 3.5
46	HSK 71	NE	2.24 (HSK 71)	3.5 ^d
50	HSK 31	NW	12.24 (HSK 31)	6.3 ^d
Voids ($N(\text{HI}) < 1 \times 10^{21} \text{ cm}^{-2}$)				
1	HSK 25, 31, 32	NW	9.11 (HSK 32)	4.5 - 6.3
11	HSK 31, 32, 35	NW	13.83 (HSK 31)	4.5 - 6.3
19	HSK 30	NW	0.73 (HSK 30)	3.5 - 4.5
32	HSK 10, 12	NW	20.16 (HSK 12)	3.5 - 4.5
33	HSK 47	N	13.38 (HSK 47)	3.5 - 4.5
35	HSK 35	NW	32.04 (HSK 35)	4.5 - 6.3
36	HSK 3, 5, 11	Int. Shell	26.28 (HSK 3)	2.5 - 4.5
Peak intensity at 100 μm with 8 μm emission				
8	HSK 25	NW	5.76 (HSK 25)	6.2 ^d
12	HSK 39, 41, 45	N	4.43 (HSK 45)	2.5 - 3.5
37	HSK 49, 51	N	1.45 (HSK 49)	4.5 - 6.3

^a The star forming complexes have been adopted from ?.

^b The nearest HII region is indicated inside the parentheses.

^c Estimated from ?.

^d Taken from ?.